**Proceedings of ASME Turbo Expo 2011**
**GT2011**
**June 6-10, 2011, Vancouver, British Columbia, Canada**

# GT2011-45300

# CHARACTERISTICS OF AN ULTRA-LEAN SWIRL COMBUSTOR FLOW BY LES AND COMPARISON TO MEASUREMENTS

**Matthias Kern, Svetoslav Marinov, Peter Habisreuther**
**Nikolaos Zarzalis**
Chair of Combustion Technology, Engler-Bunte-Institute
University of Karlsruhe (TH)
Kaiserstrasse 12, 76128 Karlsruhe, Germany
Tel: 0721 608 2126, Fax: 0721 608 7770
Email: Matthias.Kern@vbt.uni-karlsruhe.de,
WWW: http://www.vbt.uni-karlsruhe.de

**Antonio Peschiulli, Fabio Turrini**
AVIO S.p.A.
Via I MAggio, 56
10040 Rivalta di Torino (TO)
Italy

## ABSTRACT

*The lean combustion process is one of the most promising methods for reducing NOx emissions of jet engines. Since the risk of flash back is major for premixed concepts a diffusion flame concept is applied. In order to realize the lean condition in this concept the percentage of air flowing through the injection system and combustor dome has to be drastically increased. This leads to nozzles with a high effective area and to high volume flux in the primary zone of the combustor chamber. Such an injection system demands a particular focus towards flame stability at low load. Hence, it is essential to gain information on characteristics such as vortex breakdown, turbulent mixing and coherent structures (e.g. PVC) of the flow by means of numerical simulations. In the paper it is reported on the flow characteristics of the PERM injection system, which equips the AVIO annular combustor designed and developed within NEWAC, an integrated project co-funded by the European Commission. For this injections system RANS and LES simulations have been performed to investigate the isothermal flow field. The results are compared to detailed field measurements of velocity components and Reynolds stresses.*

## NOMENCLATURE

| | |
|---|---|
| $A$ | Area |
| $SN$ | Swirl Number |
| $S$ | Strain Tensor |
| $\dot{D}$ | Angular Momentum Flux |
| $\dot{I}$ | Axial Momentum Flux |
| $R_0$ | Nozzle Exit Radius |
| $u_0$ | Volumetric Nozzle Exit Velocity |
| $D$ | Injection System Frontal Diameter |
| $d_0$ | Nozzle Exit Diameter |
| IRZ | Inner Recirculation Zone |
| ORZ | Outer Recirculation Zone |
| PVC | Preceding Vortex Core |
| LDA | Laser Doppler Anemomentry, also LDV |
| RANS | Reynolds Averaged Navier Stokes |
| LES | Large Eddy Simulation |
| SST | Shear Stress Transport Model |

**Greek**

| | |
|---|---|
| $\nu$ | Kinematic Viscosity |
| $\Delta$ | Filter Length |

**Subscripts**

| | |
|---|---|
| prim | Primary Swirler |
| sec | Secondary Swirler |

| | |
|---|---|
| fr | Frontal Section |
| eff | Effective |
| sgs | Sub-grid Scale |
| hyd | Hydraulic Diameter |
| inlet | Swirl Cup Entry |

## INTRODUCTION

Aim of this work is to show a kinematic approach in the process of the investigation of the ultra-lean injection system concept PERM, developed together by University of Karlsruhe and AVIO Group. The first focus is set to the predictability of the flow field characteristics by two equation turbulence models, i.e. $k-\varepsilon$ and SST, in comparison to more sophisticated but concurrently much more costly models like LES. Furthermore, issues related to complex flow patterns will be discussed. In the first sections the experimental and numerical setups will be introduced. Both are referred to identical operating conditions presented in [1], however in the current work the isothermal flow is investigated. Further to that, a special focus is set on the dynamical behaviour of the combustor flow.

## EXPERIMENTAL SETUP

### Combustor configuration

The current injection system configuration has been described in more detail in our previous paper [1] , so here only an abbreviated overview will be given. An airblast atomizer has been used for the study, whose details are depicted on Figure 1. The combustion air is issued eccentrically through the primary and secondary swirl generator channels, imparting angular momentum on the air flow. Both flows of swirling air are accelerated in the inner nozzle and the outer concentric Venturi nozzle and leave the atomizer through its throat to enter the combustion space.

One of the most important parameters for the nozzle description is the swirl number, which is defined as the ratio of angular momentum flux divided by axial momentum flux normalized by a characteristic length dimension of the nozzle, e.g. as given by Gupta [2].

$$SN = \frac{\dot{D}}{\dot{I} \cdot R_0} \tag{1}$$

For the formation of a relevant IRZ a swirl number of at least 0.5-0.6 is required, according to Maier [3]. The theory of its occurrence through vortex breakdown mechanism is described in numerous works, for example Maier [3], Merkle [4]. In this particular study a nozzle with overall swirl number of 0.76 has been used. For determining of the overall swirl number, information about $A_{inlet,prim}$ and $A_{inlet,sec}$ is required, according to Kerr et al. [5].

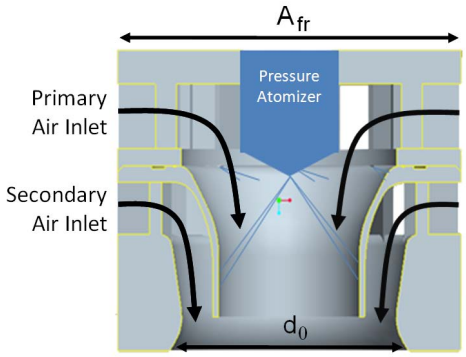


Figure 1. Axial section view of the investigated airblast atomizer

Another important parameter to characterize the nozzle is the effective area $A_{eff}$. The new concept PERM is distinguished by an excessive amount of air through the swirl cup, so the effective area is approximately three times the effective area of conventional flares.

The flow expansion ratio $D/d_0$ influences the flow topology [6] [7] [8], for this burner configuration this quantity amounts 2.5. The nozzle area ratio, expressed by the nozzle effective area $A_{eff}$ and its frontal surface $A_{fr}$ is as high as 0.22 and limits the maximum swirl applicable, due to restrictions in mounting space in the AVIO gas turbine combustion chamber.

Although the current study is carried out at isothermal conditions, a short description of the fuel supply will be given. The kerosene is issued through a pressure atomizer which provides a hollow cone spray within the nozzle. This spray hits the inner wall of the nozzle where a liquid kerosene film is built. The kerosene film is shear-driven by the air flow to the atomization lip where its disintegration into ligaments and droplets takes place, which participate at the combustion after evaporation. This atomizer is integral part of the assembly also for the isothermal case.

### Test Rig and Infrastructure

The test rig is designed to operate at ambient pressure. The most important feature is the possibility for axial movement of the nozzle holder within the chamber. The combustion chamber and the applied measurement apparatus are fixed in axial direction, while the nozzle can be axially driven, so traversing at various axial positions is possible.

In the current lab rig the combustion chamber is tubular and is insulated with ceramic material on the inner side. In radial direction insertions for different kinds of measurement technique are

prepared, also including exhaust gas and thermocouple probes. For the current study only laser optical measurements in terms of 3D LDA have been performed. For this purpose flat windows are arranged particularly for optical access inside the chamber (see Figure 2). Slits in the ceramic material are cut in specific manner to match the windows and to guarantee the optical access, thus minimal wall disturbance on the flow results. However, measurements only across the radial range are possible with this configuration and thus symmetry assumptions have been made. The arrangement is illustrated on Figure 2.

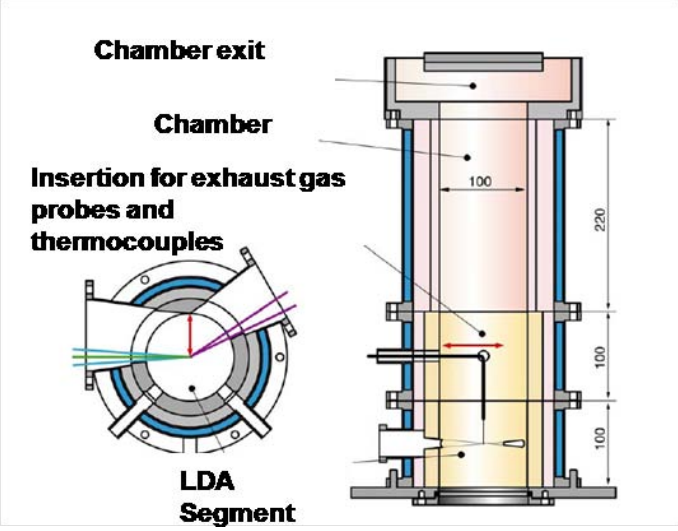


Figure 2. Combustion chamber arrangement

## Measurement techniques

The 3D velocity field has been acquired using a LDA Dantec measurement system and a Coherent argon ion laser. The optical system is shown in figure 3. Both optics are mounted on a movable frame perpendicular to the axis of the combustion chamber and can be automatically adjusted in the traversing plane by a step motor.

The LDA is a non-intrusive punctual measurement method for velocities of fluids [9] and was applied for first time in the mid 60s, shortly after Maimann [10] has invented the stimulated laser radiation. For the current investigation the LDA measurements are performed in forward scattering mode using 2 Dantec 85mm optics, as described in their documentation. Consequently the measurement volume, resulting from the beams intersection, has to remain integral throughout the duration of the measurements, thus ascertaining spatial data consistency. Another beneficial feature of the forward scattering mode arrangement is the higher light intensity in forward direction, according to Mie theory [11]. So the configuration illustrated above allows a good compromise between light intensity exploration and information content, i.e. for the third velocity component measured by the tilted optic. However, a transformation calculation for the latter is necessary to obtain its absolute velocity.

The 3D optical system is characterized by three separate colours assigned to the three velocity components. Each channel is equipped with a Bragg-cell for one of the colours, which ensures unambiguous determination of the flow direction.

The temporal resolution of the data sampling for each velocity channel varies depending on its data rate. Factors which impact this behaviour are associated with the precision of the optical arrangement, opaqueness of the chamber windows, as well as the dependency of the refraction index on the ambient temperature. The temporal coincidence is assured through a time window of 50 $\mu s$ in which a signal has to be received on all three channels.

For the LDA measurements MgO particles have been selected as seeding, because of its good thermal resistance and harmless properties. The seeding has been inserted into the combustion air flow by a particle generator. The seeding used is characterized by a median diameter of 10 $\mu m$ which is small enough to realistically reflect the flow behaviour.

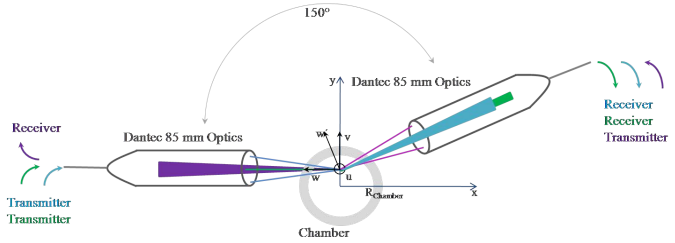


Figure 3. Optical measurement setup

## NUMERICAL SETUP

The numerical simulations have been carried out using the non-commercial CFD-library OpenFOAM release 1.5.x. This library has been published under the GNU general public licence and developed significantly in recent years. It has been extended and used successfully in recent research work [12]. Here, both LES and RANS simulations have been simulated using the OpenFOAM library. All simulations are isothermal and incompressible. For the wall treatment an analogous approach to Werner and Wenger [13] has been applied for the LES simulation while for the RANS simulations standard wall treatment using the logarithmic wall function has been used.

## Grid

For the LES simulation the grid shown in figure 4 is used. It consists of inlet plenum, primary and secondary channels, diffuser and combustion chamber. The picture in the upper left corner of figure 4 shows a front view of the simulation domain. The inlet boundary patch is marked red. On the upper right corner the grid is shown without inlet plenum, which allows to see both swirler channels. On the lower left corner a front view of the nozzle is depicted. Here the lip separating the primary and secondary air supply channel is visible. The pressure atomizer is in red color. On the lower right corner the outlet section of the domain is shown. The outlet section consists of an annular gap (red), while the center of the flame tube is blocked preventing air from flowing into the domain. The grid is unstructured and consists of 12 million hexahedral elements.

Figure 4. Various perspectives of the LES grid

For the RANS a 6° wedge shaped grid is used. The grid consists of nozzle and combustion chamber only. Primary and secondary swirl channels are not considered and the swirl is directly imposed through the boundary conditions. This procedure is necessary when using a wedge shaped mesh and has been successfully applied in various studies e.g. [12] [14]. A grid independence study has been performed and the grid has been optimized in regard to the dimensionless wall distance $Y^+$. The final mesh is shown in figure 5.

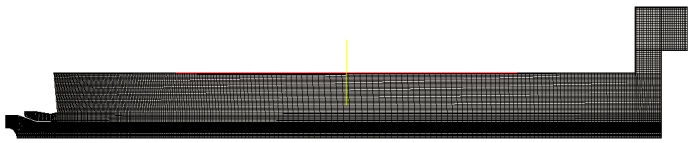

Figure 5. RANS grid

## Solver

For the LES simulation a standard Smagorinsky approach [15] has been used. The Smagorinky constant is $c_k = 0.02$ , defined by:

$$\nu_{sgs} = c_k \cdot \Delta^2 \cdot |S| \tag{2}$$

The equations are solved in a segregated manner. For the pressure correction step a PISO [16] algorithm has been used and the pressure equation is solved using a preconditioned linear solver [17], which drastically decreases the necessary iteration steps in the pressure correction. The convection terms are discretized using a filtered linear scheme, which is of second order in accuracy.

For the RANS simulations the standard $k-\varepsilon$ [18] and the shear stress transport model (SST) [19] have been applied using standard constants. The equations are solved in a segregated manner as well and the pressure correction step is solved using the SIMPLE [20] algorithm. Details to the implementation of PISO and SIMPLE within OpenFOAM can be found in [21]. The convection terms are discretized using the Gamma scheme [22], which is a blending between upwind and central differencing using a NVD (Normalized Variable Diagram) criterion and is second order in accuracy.

For all simulations a Neumann boundary condition has been chosen for the velocity at the inlet patch and a Dirichlet boundary condition for the outlet section. Vice versa, the total pressure is fixed at the outlet and a Neumann boundary condition for the static pressure is used at the inlet. Since the turbulence is mainly formed within the swirler channels, the flow enters the LES simulation domain at the plenum inlet laminar. In the RANS context a turbulence intensity of 10% and a turbulent length scale of $l_t = \frac{1}{4} \cdot d_{hyd}$ is assumed at the inlet section of the nozzle. The LES runs for 1 million iteration steps at a time step of $2. \cdot 10^{-7} s$, which correspondes to a maximum Courant number of $< 0.2$. The RANS simulations are performed in steady state condition and are assumed to be converged at a maximum residuum of $1 \cdot 10^{-5}$ for each equation.

## RESULTS AND DISCUSSION

In this section the results of both measurement and simulation are presented. First the normalized mean axial velocities are discussed outlining the main pattern of the flow, illustrated in figures 6 and 7. The figures contain normalized axis, with the normalization factor being the nozzle exit radius $R_0$. The mean axial velocity is normalized by the volumetric nozzle exit velocity $u_0$. Also the stagnation isolines are shown, depicting inner (IRZ) and outer (ORZ) recirculation zones. The axial position $x/R_0 = 0$ represents the nozzle exit, however the first axial measurement has been carried out slightly downstream due to geometrical reasons. Generally on both figures the similar flow topology can be recognized, consisting of main flow, inner and outer recirculation zones.

However, the RANS results using the SST model exhibit significant deviations concerning shape of the inner recirculation zone and its intensity, especially adjacent to the nozzle exit. Also the curvature of the stagnation line in the vicinity of the nozzle differs. While the measurement shows a convex shape the SST model predicts a concave shape in this regard. This matter also implies the shape of the main flow. While the IRZ almost closes on the center line after a distance of approximately 2.5 radii, the simulated IRZ is bubble shaped. The intensity of the recirculation flow is significantly higher for both inner and outer recirculation zones in the simulated case. This may have important impact in regard to flame stability simulations.

Oppositely, the LES simulation shows a good agreement in terms of shape and recirculation intensity in the IRZ as can be seen in figure 7. This can be seen especially directly at the nozzle exit. Figures 8 to 11 show radial profiles of all three mean velocity components. The first and last line plot represent the lower and upper boundaries of the measured range, respectively. Figure 8 illustrates the good match of the LES and measurement results. At the same time RANS exhibits significant deviations in the area of the inner recirculation. However, in regard to radial and tangential velocity the match between RANS and experiment is good as well. This justifies the boundary conditions, i.e. neglecting the swirl channels‘ geometry and directly imposing the swirl to the nozzle entry section. However, with further propagating of the flow downstream the RANS simulation shows a tendency to transport the tangential velocity faster to bigger radii, while LES still represents very good agreement. As expected at the end of the investigated range far enough from the nozzle, all the velocity profiles have flattened. Nevertheless, it can be recognized that for the mean tangential velocity LES still is in better agreement with the experimental data.

Since LES is the only model capable of predicting the IRZ shape correctly, only these results are considered in the further discussion. An interesting finding can be seen in the characteristics of the Reynold's stresses illustrated in figures 12 to 14. The stresses are in good agreement between simulation and measurement except for the magnitude in the shear layer close to nozzle.

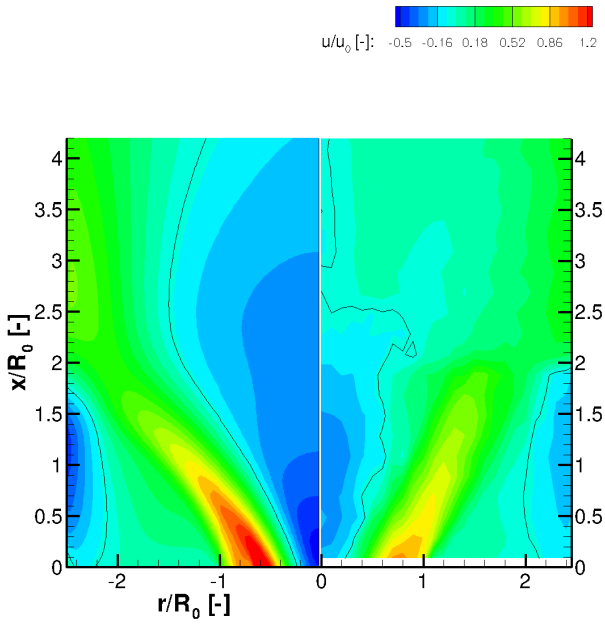


Figure 6. Comparison of normalized axial mean velocity of SST RANS simulation (left) and measurement (right)

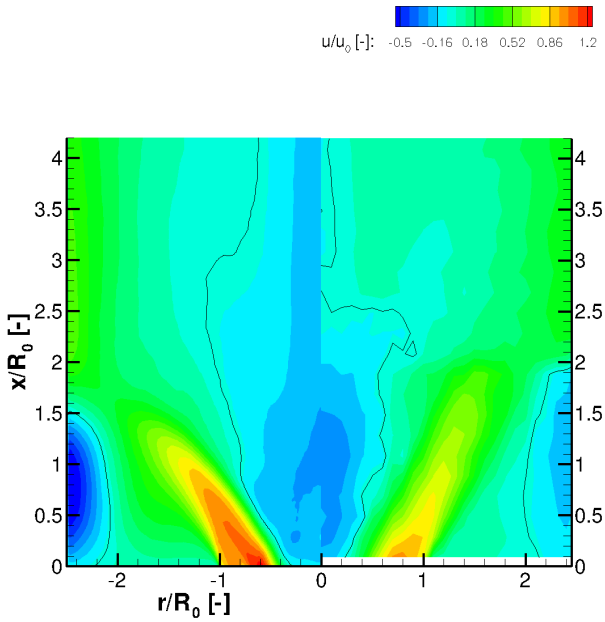


Figure 7. Comparison of normalized axial mean velocity of LES simulation (left) and measurement (right)

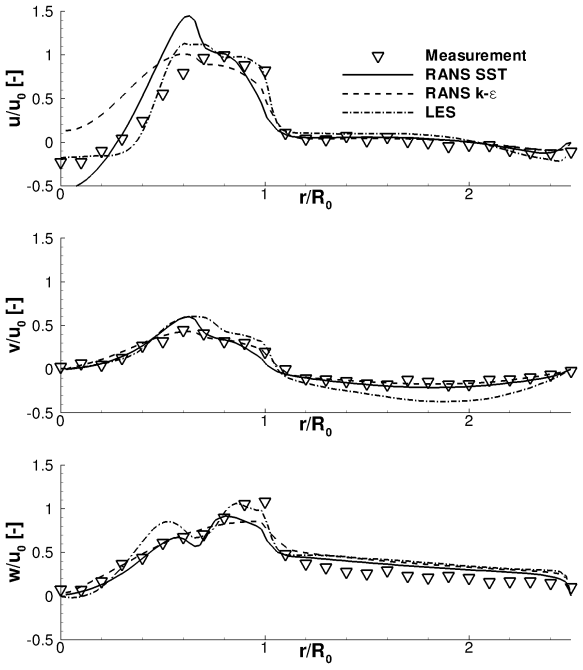


Figure 8. Mean velocities at a distance of $x/R_0 = 0.0875$ from the nozzle exit

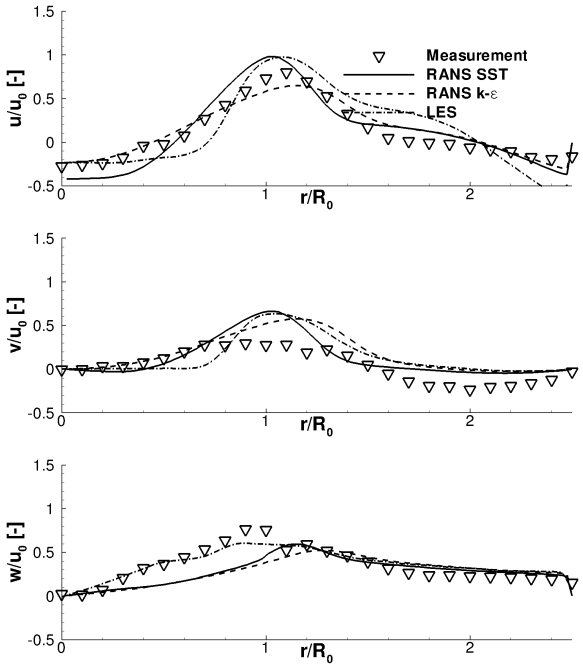


Figure 9. Mean velocities at a distance of $x/R_0 = 0.6875$ from the nozzle exit

Additionally, especially in this region a strongly dominant coherent structure can be seen in the simulated flow field. Figure 15 shows a 3D pressure iso contour at a pressure level of $9.7 \cdot 10^4 Pa$, thus depicting a region of underpressure. This helical structure is well known in literature as PVC (Preceding Vortex Core) [23] [24] [25]. In the current case of PERM characterized by high volume flux this PVC is particularly intensive and has a high frequency. Figure 15 shows a compact, undistorted inner structure of the PVC, while in its surroundings more wrinkled turbulent structures can be seen in figure 16. This anticipated intensity is particularly well depicted by the pressure field shown in figure 17. The PVC is located on top of the pressure atomizer within the nozzle and exhibits a maximum differential pressure of up to 35%. This finding reflects also the calculated instantaneous velocity field shown in figure 18 where high gradients of up to twice the volumetric velocity can be seen across the vortex structure.

For further investigation a FFT of the axial velocity at a probe point within the PVC has been performed within a time range of 0.0158s and with a time step of $2 \cdot 10^{-7} s$. This corresponds approximately 80000 iteration steps. The resulting flow spectrum is given in figure 20. The spectrum shows a dominant frequency of 1560 Hz.

This result has been obtained by means of LDA measurement as well, shown in our previous publication [26]. However, a high sampling frequency is required to resolve the above mentioned structure, which could be achieved by only evaluating the signal on the LDA processor for the axial velocity signal. The reason for doing so is that the 3D measurement implies a coincidence requirement, i.e. the coexistence of all three velocity signals within a time window of $50\mu s$. Thus, cutback of the sampling frequency occurs and is not sufficient to resolve the frequency.

Nevertheless, the experimental results show a very good agreement in frequency of 1545Hz measured to 1560Hz simulated. The fact that this influences the spray structure and hence the combustion has been shown in [26]. The influence on the spray structure has been investigated through high speed imaging and is shown in figure 19. The spray oscillation shows the same frequency as the PVC. This is further emphasized by the intense pressure and velocity fluctuations produced by the PVC as presented above in the current paper.

In the simulation it is possible to resolve the frequency of PVC, and due to its high amplitude it is considered to be the main source for the calculated stresses adjacent to the nozzle exit. Contrary, this behaviour can not be resolved by the current experiment and thus the obtained stresses are lower. Assuming this reduced sampling frequency to remain constant for the whole duration of one measurement point, it would not be possible to resolve this PVC. However, here the sampling rate varies with time. So, this frequency would be obtained after a statistically sufficient number of samples, which requires much longer measurement time compared to flows without dominant high frequency

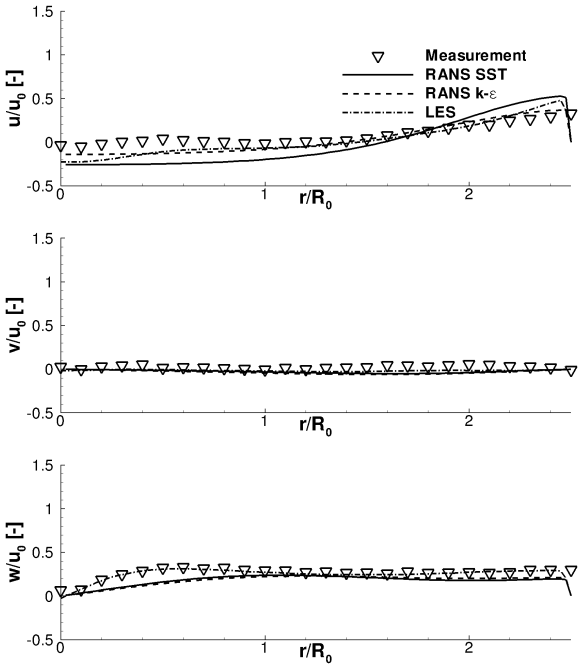


Figure 10. Mean velocities at a distance of $x/R_0 = 2.8875$ from the nozzle exit

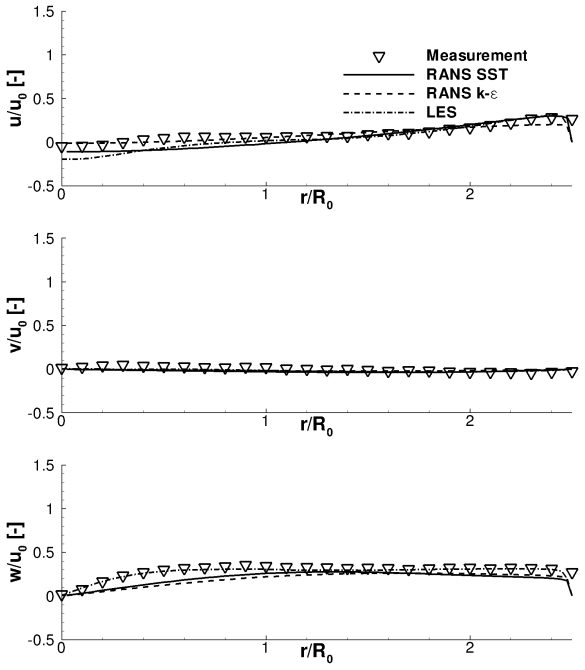


Figure 11. Mean velocities at a distance of $x/R_0 = 5.0875$ from the nozzle exit

coherent structures.

## CONCLUSIONS

The flow field produced by the ultra-lean PERM swirl cup has been compared by means of simulation and measurement. It has been shown that only highly sophisticated models as LES are capable to correctly predict the mean flow field. Especially shape and intensity of the IRZ, which plays a key role for combustion stability, is significantly better predicted by LES than RANS. The shape of the normal Reynolds stresses is also matched by LES, however discrepancies in terms of magnitude are visible in the region close to the nozzle. In this region a high frequent, dominant coherent structure (PVC) can be identified by means of LES. This structure can be detected as well using only the axial LDA signal due to the drawback of the coincidence requirement of 3D LDA. Due to its high frequency and amplitude this structure is considered as main source for the discrepancies regarding the magnitude of the Reynolds stresses as discussed above. For a better comparison the measurement has to be improved by increasing the measurement time at selected measurement positions where the PVC occurs. Nevertheless, the existence of this structure can be proved only by both numerical and experimental approach. In the current investigation this dynamic behaviour has a significant impact on the combustion and has to be considered of outstanding importance.

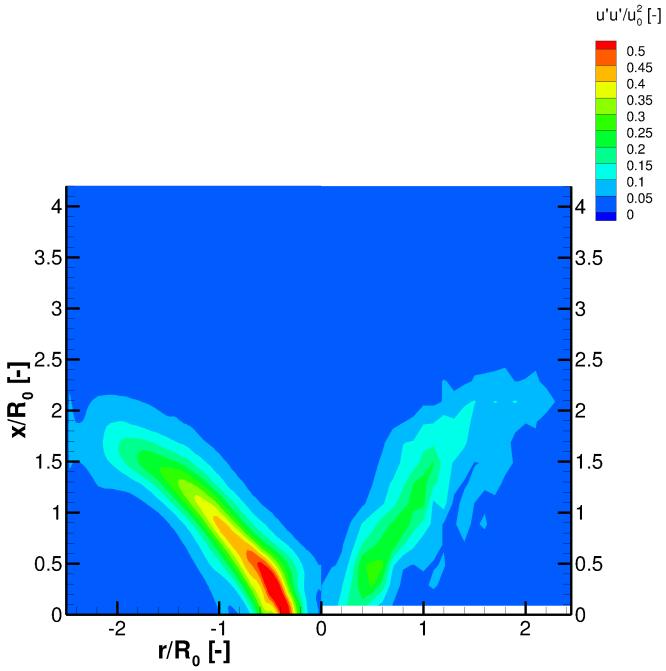


Figure 12. Numerically and experimentally resolved normal Reynolds' stresses $\overline{u'u'}$

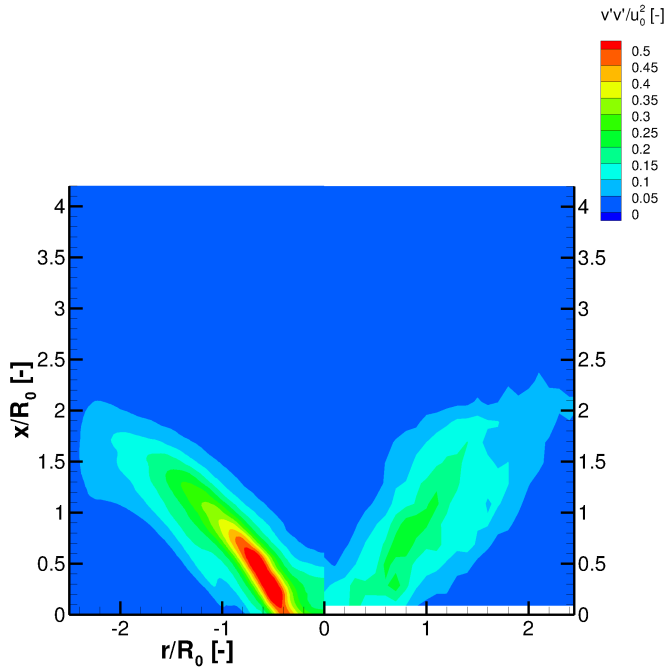


Figure 13. Numerically and experimentally resolved normal Reynolds' stresses $\overline{v'v'}$

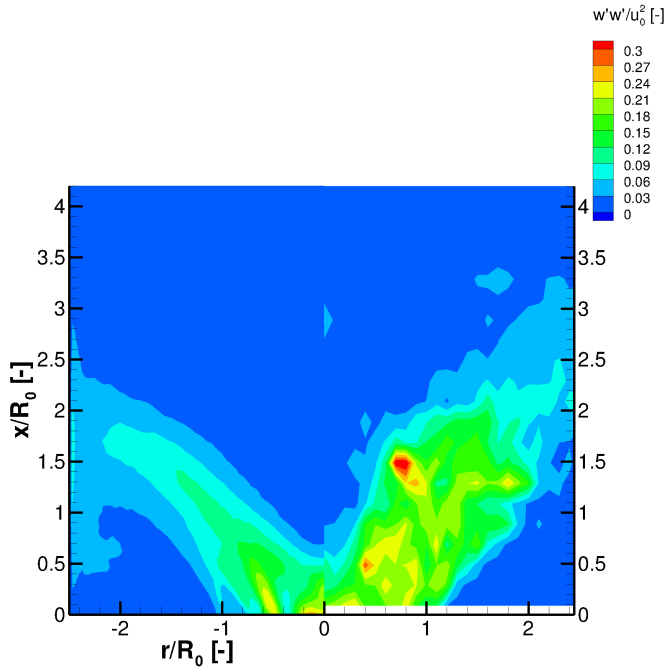


Figure 14. Numerically and experimentally resolved normal Reynolds' stresses $\overline{w'w'}$

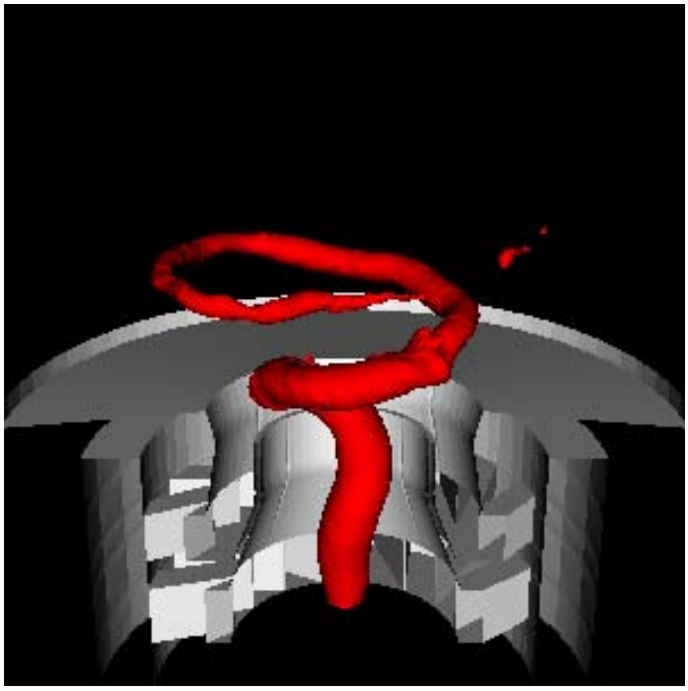

Figure 15. Pressure iso contour at a pressure level of $9.7 \cdot 10^4 Pa$

Figure 16. Pressure iso contour at a pressure level of $1 \cdot 10^5 Pa$

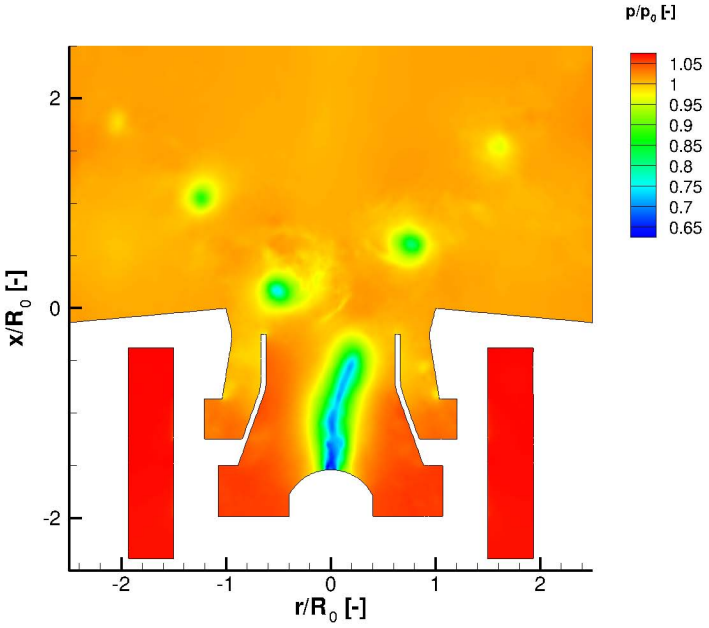


Figure 17. Instantaneous simulated pressure field

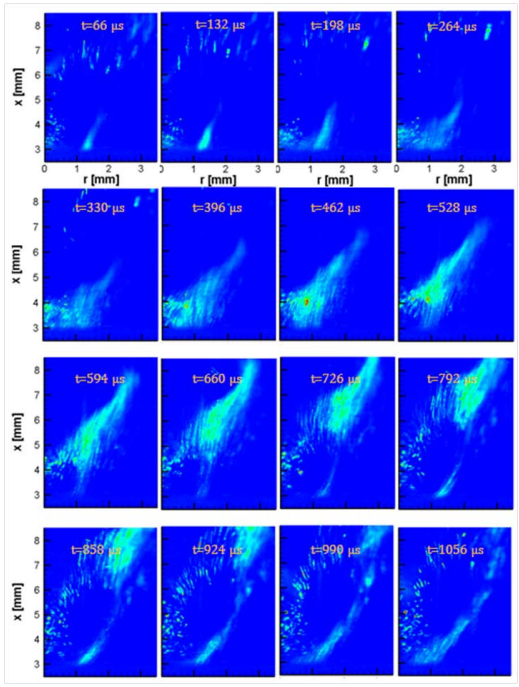


Figure 19. Dynamic spray behaviour from high speed imaging

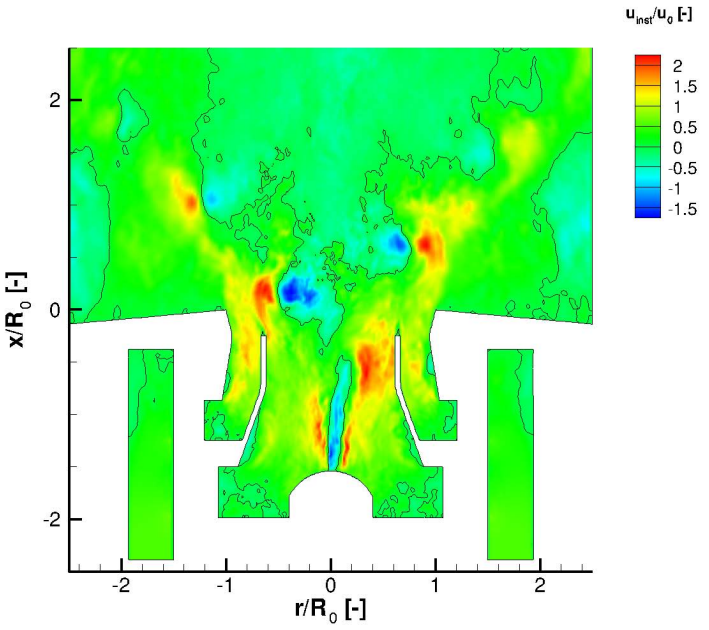


Figure 18. Instantaneous simulated velocity field

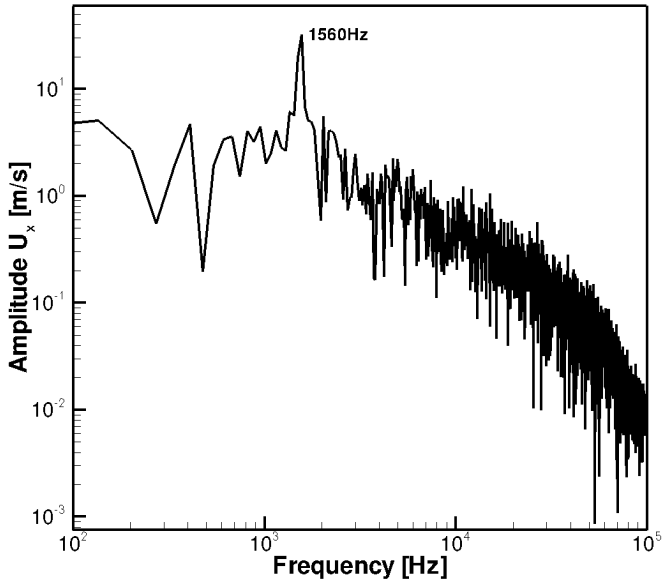


Figure 20. Flow spectrum for the axial velocity

## ACKNOWLEDGMENT

We kindly acknowledge financial support by the European Commission through project NEWAC (Contract No. AIP5-CT-2006-030876).

## REFERENCES

[1] Marinov, S., Kern, M., Zarzalis, K. M. N., Peschiulli, A., and Turrini, F., 2010. "On swirl stabilized flame characteristics near the weak extinction limit". In Proceedings of ASME Turbo Expo 2010.

[2] Gupta, A. K., 1984. *Swirl Flows*. Cambridge: Abacus Press.

[3] Maier, P., 1967. "Untersuchung turbulenter isothermer drallstrahlen und turbulenter drallflammen". PhD thesis, University of Karlsruhe, Engler-Bunte-Institut, Chair of Combustion Technology.

[4] Merkle, K., 2006. "Einfluss gleich- und gegensinniger drehrichtung der verbrennungsluftströme auf die stabilisierung turbulent doppeldrall-diffusionsflammen". PhD thesis, University of Karlsruhe, Engler-Bunte-Institut, Chair of Combustion Technology.

[5] Kerr, N. F., 1965. "Swirl part i: Effect on axisymmetrical turbulent jets". *Journal of the Institute of Fuel*, pp. 519–526.

[6] Thring, M. W., 1953. "Combustion length of enclosed turbulent jet flames". In Fourth Symposium on Combustion, pp. 785–796.

[7] Fanaca, D., Alemela, P. R., Hirsch, C., Sattelmayer, T., and Schuermans, B., 2009. "Comparison of the flow field of a swirl stabilised premixed burner in an annular and a single burner combustion chamber". In Proceedings of ASME Turbo Expo 2009.

[8] Fu, Y., Cai, J., Jeng, S.-M., and Mongia, H., 2005. "Confinement effects on the swirling flow of a counter-rotating swirl cup". In Proceedings of ASME Turbo Expo 2005.

[9] Ruck, B., 1987. *Laser-Doppler-Anemometrie*. Stuttgart: AT-Fachverlag GmbH.

[10] Maimann, T., 1960. "Optical maser action in ruby". *Nature,* **187**, pp. 493–494.

[11] Mie, G., 1908. "Beiträge zur Optik trüber Medien, speziell kolloidaler Metallösungen". *Anal. d. Physik,* **25**(4).

[12] Kern, M., Fokaides, P., Habisreuther, P., and Zarzalis, N., 2009. "Applicability of a flamelet and a presumed jpdf 2-domain-1-step-kinetic turbulent reaction model for the simulation of a lifted swirl flame". In Proceedings of ASME Turbo Expo 2009.

[13] Werner, H., and Wengle, H., 1991. "Large-eddy simulation of turbulent flow over and around a cube in a plate channel". In 8th Symposium on Turbulent Shear Flows, pp. 155–168.

[14] Brunn, O., Wetzel, F., Habisreuther, P., and Zarzalis, N., 2006. "Investigation of a combustor using a presumed jpdf reaction model applying radiative heat loss by the monte carlo method". In Proceedings of the 25th Congress of the International Council of the Aeronautical Sciences (ICAS 2006).

[15] Smagorinsky, J., 1963. "General circulation experiments with the primitive equations". *Monthly Weather Review,* **91**, pp. 99–164.

[16] Issa, R., 1985. "Solution of the implicitly discretised fluid flow equations by operator-splitting". *Journal of Computational Physics,* **62**, pp. 40–65.

[17] Hrvoje Jasak, Aleksandar Jemcov, J. P. M., 2007. Preconditioned linear solvers for large eddy simulation. Tech. rep., University of Zagreb.

[18] Jones, W. P., and Launder, B. E., 1972. "The prediction of laminarization with a two-equation model of turbulence". *International Journal of Heat and Mass Transfer,* **15**, pp. 301–314.

[19] Menter, F. R., 1994. "Two-equation eddy-viscosity turbulence models for engineering applications". *AIAA Journal,* **32**, pp. 1598–1605.

[20] S. V. Patankar, D. B. S., 1972. "A calculation procedure for heat, mass and momentum transfer in three-dimensional parabolic flows". *Int. J. Heat Mass Transfer,* **15**, pp. 1787–1806.

[21] Jasak, H., 1996. "Error analysis and estimation for the finite volume method with applications to fluid flows". PhD thesis, University of London.

[22] H. Jasak, H.G. Weller, A. G., 1999. "High resolution nvd differencing scheme for arbitrarily unstructured meshes". *International Journal for Numerical Methods in Fluids,* **31**, pp. 431–449.

[23] Syred, N., 2006. "A review of oscillation mechanisms and the role of the precessing vortex core (pvc) in swirl combustion systems". *Progress in Energy and Combustion Science,* **32**, pp. 93–161.

[24] Boileau, M., Pascaud, S., Riber, E., Cuenot, B., Gicquel, L. Y. M., Poinsot, T. J., and Cazalens, M., 2008. "Investigation of two-fluid methods for large eddy simulation of spray combustion in gas turbines". *Flow, Turbulence and Combustion,* **80**, pp. 291–321.

[25] Martin Freitag, M. K., 2005. "Direct numerical simulation of a recirculating swirling flow". *Flow, Turbulence and Combustion,* **75**, pp. 51–66.

[26] Marinov, S., Kern, M., Zarzalis, N., Turrini, F., and Peschiulli, A., 2010. "Spray characteristic investigation of a kerosene fuelled swirl flame". In Proceedings of SPEIC10.